BNL-223349-2022-JAAM

In Situ Growth of Crystalline and Polymer-Incorporated Amorphous ZIFs in Polybenzimidazole Achieving Hierarchical Nanostructures for Carbon Capture

L. Hu, K. Kisslinger

To be published in "SMALL"

May 2022

Center for Functional Nanomaterials

Brookhaven National Laboratory

U.S. Department of Energy

USDOE Office of Science (SC), Basic Energy Sciences (BES) (SC-22)

DISCLAIMER

In situ synergistic growth of crystalline and polymer-incorporated amorphous ZIF-8 in polybenzimidazole achieving hierarchical nanostructrues for H_2/CO_2 separation

*Leiqing Hu†, Vinh T Bui†, Sankhajit Pal, Wenji Guo, Ashwanth Subramanian, Kim Kisslinger, Shouhong Fan, Chang-Yong Nam, Yifu Ding, Haiqing Lin**

Dr. L. Hu, V.T. Bui, S. Pal, Dr. W. Guo, Prof. Dr. H. Lin
Department of Chemical and Biological Engineering
University at Buffalo, The State University of New York
Buffalo, NY 14260, USA
E-mail: haiqingl@buffalo.edu

K. Kim, Dr. C.-Y. Nam
Center for Functional Nanomaterials
Brookhaven National Laboratory
Upton, NY 11973, USA

A. Subramanian, Prof. C.-Y. Nam
Department of Materials Science and Chemical Engineering
Stony Brook University
Stony Brook, NY 11794, USA

S. Fan, Prof. Dr. Y. Ding
Department of Mechanical Engineering
University of Colorado
Boulder, CO 80309, USA

Abstract: Mixed matrix materials (MMMs) hold great potential for membrane gas separations by merging nanofillers with unique nanostructures and polymers with excellent processability, but their promise is often hampered by interfacial incompatibility leading to voids and thus deleterious selectivity. Herein we demonstrate in-situ synergistic growth of **c**rystalline zeolite imidazole framework-8 (ZIF-8) and **p**olymer-incorporated **a**morphous ZIF-8 in polybenzimidazole (PBI)-based **M**MMs (CPAMs) with superior H_2/CO_2 separation performance. The amorphous ZIF-8 (enabled by the benzimidazole groups on the PBI backbones with a structure similar to the precursor for ZIF-8, i.e., 2-methylimidazole) improves interfacial compatibility and tightens the PBI nanostructures, while the highly porous crystalline ZIF-8 nanoparticles render high gas permeability. The formation of 24 mass% ZIF-8 in PBI improves both H_2 permeability and H_2/CO_2 selectivity, overcoming the conventional permeability/selectivity tradeoff. This work unveils a new platform of MMMs based on functional polymer-incorporated amorphous ZIFs exhibiting superior interfacial compatibility and hierarchical nanostructures for a variety of applications.

1. Introduction

Hydrogen (H_2) has attracted significant attention as a clean energy source to mitigate the CO_2 emissions to the atmosphere. Clean H_2 can be produced at a large scale by reforming or gasification of fossil fuels, and the byproduct CO_2 must be captured for utilization or sequestration.[1] Membrane technology has been extensively investigated for H_2/CO_2 separation due to its high energy efficiency, and membrane materials with strong size-sieving ability are pursued because H_2 has a smaller kinetic diameter (2.89 Å) than CO_2 (3.3 Å).[2] With excellent processability, polymers with low free volume and rigid architectures can be designed to achieve strong size-sieving ability. However, their amorphous structure and irregular free volume elements

can not provide sharp molecular sieving, and the low free volume leads to low H_2 permeability.[2b, 3] By contrast, inorganic membranes with well-defined pore sizes have been demonstrated to have very high H_2/CO_2 selectivity, including silica,[1b, 4] zeolites,[5] graphene oxide (GO),[6,7] carbon molecular sieves,[7] and zeolite imidazole frameworks (ZIFs).[8] However, the fabrication of these defect-free nanostructured membranes at an industrial scale remains a substantial challenge.

Dispersion of the nanofillers in polymers integrates unique properties in nanoporous materials with excellent processability of polymers, rendering a versatile and practical materials platform for a variety of applications, including membranes for gas separation[9] and liquid separation,[10] proton/anion exchange membranes for fuel cells,[11] polymer electrolytes for Li-ion batteries,[12] and thermal conductors.[13] Particularly, ZIFs have been widely used for gas separation membranes due to their good compatibility with polymers induced by the organic ligands and their suitable aperture sizes (such as 3.4 Å for ZIF-8 and 3.0 Å for ZIF-7).[14] Nevertheless, the obtained mixed matrix materials (MMMs) do not exhibit high H_2/CO_2 selectivity, presumably because of the micro-defects caused by the interfacial incompatibility at high loadings.[14-15] The ZIFs can be synthesized in-situ in polymers to improve interfacial compatibility.[9d, 16] However, the resulting MMMs display gas separation performance similar to those traditional MMMs.[16c, 16d, 17]

Herein we demonstrate a new approach of in-situ growth of ZIFs to enhance both interfacial compatibility and H_2/CO_2 separation performance, where functional polymers containing the ligands to form the ZIFs on the backbones are used to form amorphous ZIF-8 (*a*ZIF-8). Specifically, the precursors of ZIF-8 (i.e., $Zn(NO_3)_2 \cdot 6H_2O$ and 2-methylimidazole or 2-mIm) are dispersed in a solution of polybenzimidazole (PBI) containing benzimidazole (bIm) with a structure similar to 2-mIm. The in situ growth results in crystalline ZIF-8 (*c*ZIF-8) and amorphous *a*ZIF-8 incorporating 2-mIm and bIm, as shown in Figure 1. The unreacted precursors in the films

can be removed by methanol washing. The obtained MMMs are named CPAM-*xx*, where *xx* represents the mass percentage (mass%) of the synthesized *a*/*c*ZIF-8 (Tables S1 and S2).

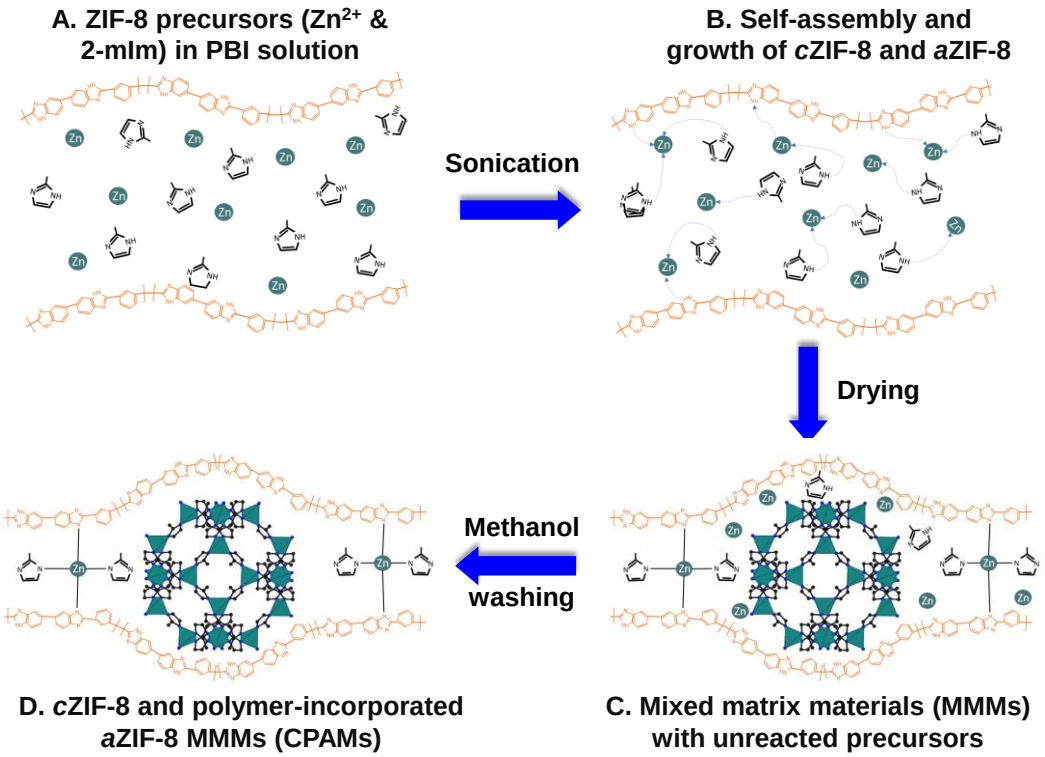

Figure 1. Schematic illustration of in situ growth of *c*ZIF-8 NPs and *a*ZIF-8 incorporating 2-mIm and bIm from the PBI backbones.

We thoroughly investigated the chemical and structural characteristics of the CPAMs. The incorporation of *c*ZIF-8 nanoparticles (NPs) increases free volume and thus gas permeability, while the formed *a*ZIF-8 cross-links the PBI chains and decreases the free volume, increasing the size-sieving ability and thus H_2/CO_2 selectivity. The resulting hierarchical nanostructures simultaneously improve H_2 permeability and H_2/CO_2 selectivity, thereby overcoming the permeability/selectivity tradeoff. CPAM-15 exhibits the best H_2/CO_2 separation properties among all the CPAMs, and when challenged with simulated syngas, it exhibits stable and superior H_2/CO_2 separation properties, surpassing Robeson's upper bound. Amorphous ZIFs have emerged as an

interesting material platform,[18] and this work for the first time demonstrates its synergy with the *c*ZIF to create suitable nanostructures for gas separations.

2. Results and discussion

Chemical and nanostructural properties of CPAMs: Figure 2A displays the Fourier-transform infrared (FTIR) spectra of the CPAMs. Compared with PBI (or CPAM-0), CPAM-3.4, CPAM-15, and CPAM-24 display new peaks at 1140 and 990 cm^{-1} that are characteristics for the C−N groups in the ZIF-8 spectrum (cf. Figure S1a), indicating the growth of *c*ZIF-8 NPs in these MMMs.[15] The peak at 1630 cm^{-1} representing the N−H groups of the imidazole ring on the PBI chains decreases sharply in the spectra of CPAM-15 and CPAM-24, confirming the strong interaction between the imidazole ring and Zn^{2+} ions, which cross-link the PBI chains.[19] However, the produced Zn−N bonding with a characteristic peak of 421 cm^{-1} cannot be distinguished from other peaks.[20]

The total content of Zn^{2+} ion in three CPAMs and its distribution in *a*ZIF-8 and *c*ZIF-8 were determined, and the results are summarized in Table S2. The molar ratios of Zn atom to 2-mIm in the CPAMs are ≈ 0.5, the same as that in *c*ZIF-8, suggesting that *a*ZIF-8 also has the Zn:2mIm ratio of 0.5 (cf. Figure 1C).[18b, 21] Moreover, the molar ratio of Zn^{2+} in *a*ZIF-8 to *c*ZIF-8 ranges from 2.1 for CPAM-3.4 to 1.4 for CPAM-24, indicating a dominant role of the *a*ZIF-8 and its decreasing influence with increasing ZIF-8 content. Neverthless, a significant portion of Zn^{2+} is available to coordinate with bIm on the PBI backbones.[22] For instance, CPAM-24 has a molar ratio of Zn^{2+} in the *a*ZIF-8 to bIm of 0.12, leading to highly coordinated networks and high cross-linking degree.

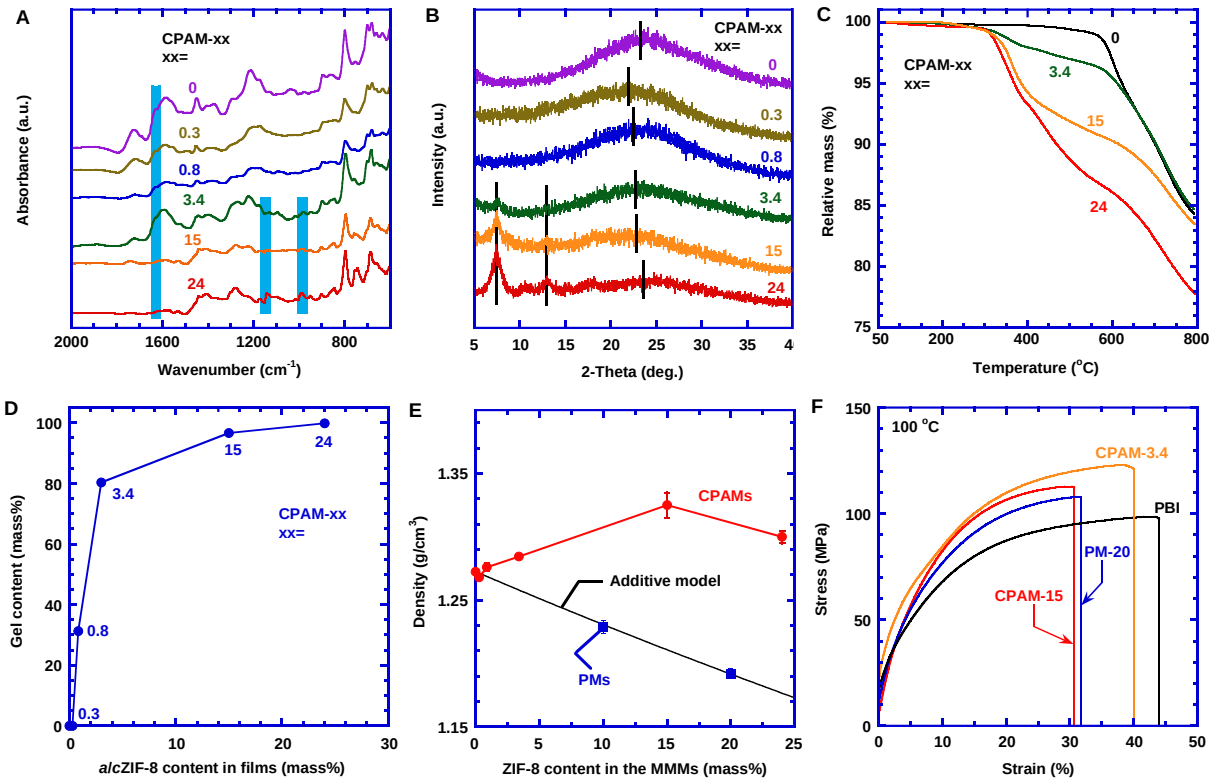

Figure 2. Chemical and structural characterization of the CPAMs. (A) FTIR spectra; (B) WAXD patterns; (C) TGA curves; (D) gel content; (E) density; and (F) stress-strain tensile plots at 100 °C.

To elucidate the advantage of the CPAMs, MMMs comprising *c*ZIF-8 NPs and PBI were prepared via the post-synthesis mixing method and named as PM-*yy*, where *yy* represents the mass percentage of *c*ZIF-8 in the films (Tables S1 and S2). PM-10 and PM-20 display a strong peak at 1630 cm^{-1} presenting N−H groups on the imidazole ring (cf. Figure S1a), indicating that Zn^{2+} ions on the post-synthesized ZIF-8 have no special interaction with the amine groups on imidazole rings of PBI chains as they are saturated by 2-mIm.

Figure 2B presents the wide-angle X-ray diffraction (WAXD) patterns of the CPAMs. The CPAMs exhibit two characteristic peaks of 7.5° and 13° for crystalline ZIF-8 (cf. Figure S1b), confirming the existence of *c*ZIF-8. PBI displays a broad peak at 23.2°, which corresponds to a *d*-spacing (representing the average inter-segmental distance between the polymer chains) of 3.8 Å calculated using Bragg's equation.[23] Increasing the *c*/*a*ZIF-8 loading increases the *d*-spacing

(caused by the ZIF-8 NPs-induced disruption of the chain packing) before decreasing due to the increased *a*ZIF-8 content and degree of PBI cross-linking.

Figure 2C compares the thermal stability of three CPAMs with PBI. PBI and PM-20 are stable until 500 ℃ and then degrades rapidly at 550 ℃ (cf. Figure S1c,d), similar to the previous study.[24] By contrast, CPAMs start to degrade at 300 ℃ because of the loss of 2-mIm from the *a*ZIF-8, which appears to be completed at ≈ 480 ℃, according to the derivative thermogravimetric analysis (DTA) curves (Figure S2). The *a*ZIF-8 is not as thermally stable as *c*ZIF-8.[25] On the other hand, the 2-mIm in *a*ZIF-8 is more stable than its pure crystalline form with a boiling point of 268 ℃ due to its strong interactions with Zn^{2+} ions.[31]

The gel content of the CPAMs was measured by immersing the samples in DMF at 35 ℃ for 24 h to illustrate the effect of the formed *a*ZIF-8. Same as PBI, CPAM-0.3 can be completely dissolved in DMF due to the low content of Zn^{2+} ions. In contrast, CPAM-0.8 displays a gel content of 31±1% (cf. Table S3), indicating that the Zn^{2+}-bIm coordination (derived from *a*ZIF-8 or even the ligand exchange of *c*ZIF-8[26]) cross-links the PBI chains. Increasing the Zn^{2+} content increases the gel content, as shown in Figure 2D. For example, CPAM-24 has a gel content near 100%, suggesting the complete cross-linking of the PBI chains. Interestingly, PM-20 also shows a gel content of 22±1% (Table S4), probably because of the ligand exchange between 2-mIm and bIm on the PBI backbones.[26] Nevertheless, the gel content in PM-20 is much lower than that in the CPAM-24 despite their similar ZIF-8 content.

Figure 2E compares the density of the CPAMs and PMs (cf. Table S3). The density of the PMs (ρ_S) can be well described using the additive model,[15] $1/\rho_S = w_{PBI}/\rho_{PBI} + w_{cZIF8}/\rho_{cZIF8}$, where *w* is the mass fraction for each component. The density of *c*ZIF-8 (ρ_{cZIF-8}) is 0.95 g/cm^3.[15] By contrast, the CPAMs exhibit much higher density than the PMs because of the formation of

*a*ZIF-8 and the higher ρ_{PBI} caused by the cross-linking. The *a*ZIF-8 may be assumed to have the same density as the skeletal density of the *c*ZIF-8 (1.4 g/cm^3), much higher than *c*ZIF-8.[27] Increasing the *c*/*a*ZIF-8 content in the CPAMs increases the density before decreasing probably because of the opposite effect of the increasing content of *a*ZIF-8 (increasing the density) and *c*ZIF-8 (decreasing the density). The results are consistent with the decreased ratio of *a*ZIF-8 to *c*ZIF-8 in the CPAMs.

The effect of *c*ZIF-8 and *a*ZIF-8 on the thermo-mechanical properties of the CPAMs was investigated. Figure 2F compares the stress-strain plots of PBI, CPAM-3.4, CPAM-15, and PM-20 films at 100 ℃. The detailed values are also recorded in Table S3. The break strain of CPAM-24 is only 0.66%, and its stress-strain plot is not displayed. Both CPAMs and PMs have higher Young's modulus and tensile strength but lower break strain than PBI, indicating that the *c*ZIF-8 in PBI leads to a ductile-to-brittle transition.[28] Additionally, CPAM-3.4 and CPAM-15 have higher Young's modulus and tensile strengths than PM-20, indicating that the *a*ZIF-8 and cross-linked structure produce more rigid and stiff packings of the polymer chains.

Figure 3A-E displays the scanning electron microscope (SEM) micrographs of the cross-sectional morphology of the CPAMs. The *c*ZIF-8 NPs formed in the films have uniform sizes ranging from 0.7 to 1 μm, and they are well dispersed in the films without agglomeration. The loading of *c*ZIF-8 increases from CPAM-0.3 to CPAM-24 due to the increased amount of the precursors. Interfacial voids can be observed between the PBI and ZIF-8 NPs, indicating the poor interaction between the dispersed and continuous phases. Furthermore, the distribution of the Zn element is exhibited in the in-situ mappings of energy-dispersive X-ray spectroscopy (EDS). As expected, the Zn density increases from CPAM-0.3 to CPAM-24. The uniform distribution of the Zn element confirms the good dispersion of ZIF-8 in the CPAMs. In particular, compared with

*c*ZIF-8 and PM-20 that only display Zn elements on localized positions (Figure 3F,G), CPAM-15 and CPAM-24 have uniform Zn distributions, confirming the formation of *a*ZIF-8 (Figure 3D,E).

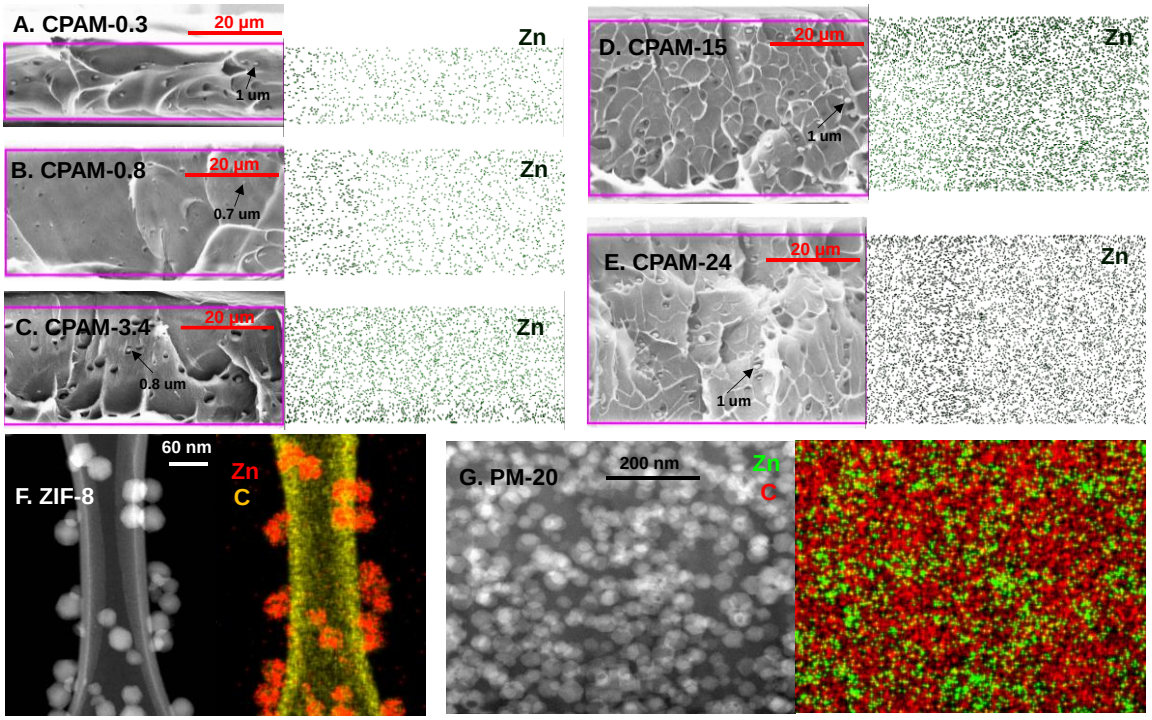

Figure 3. SEM cross-sectional images (left) of CPAMs and in-situ EDS mappings (right) of Zn element: (A) CPAM-0.3; (B) CPAM-0.8; (C) CPAM-3.4; (D) CPAM-15; (E) CPAM-24. TEM images (left) and situ EDS mappings (right) of Zn and C elements for (F) ZIF-8 and (G) PM-20 cross-section.

Pure-gas H_2/CO_2 separation properties: Figure 4A exhibits pure-gas H_2 and CO_2 permeability of CPAMs at 7.0 atm and 35 °C. PBI shows H_2 permeability of 1.9 Barrer (1 Barrer = 10^{-10} cm^3(STP) cm cm^{-2} s^{-1} $cmHg^{-1}$) and H_2/CO_2 selectivity of 14, consistent with the literature.[3b, 29] Gas permeability increases as the *a*/*c*ZIF-8 content increases to 3.4 mass% before decreasing. For instance, H_2 permeability increases to 11 Barrer for CPAM-3.4 before decreasing to 2.5 Barrer for CPAM-24. The initial increase in gas permeability can be attributed to the high porosity and thus extremely high permeability of the *c*ZIF-8 (i.e., H_2 and CO_2 permeability of 22,000 and 3,300 Barrer, respectively).[15, 30] As a result, PM-20 exhibits H_2 permeability of 29 Barrer, much higher

than PBI (Table S4). The decreased permeability with the *a*/*c*ZIF-8 content of 15 mass% or higher can be ascribed to the increased amount of *a*ZIF-8, which decreases the *d*-spacing and free volume and spans throughout the whole films.

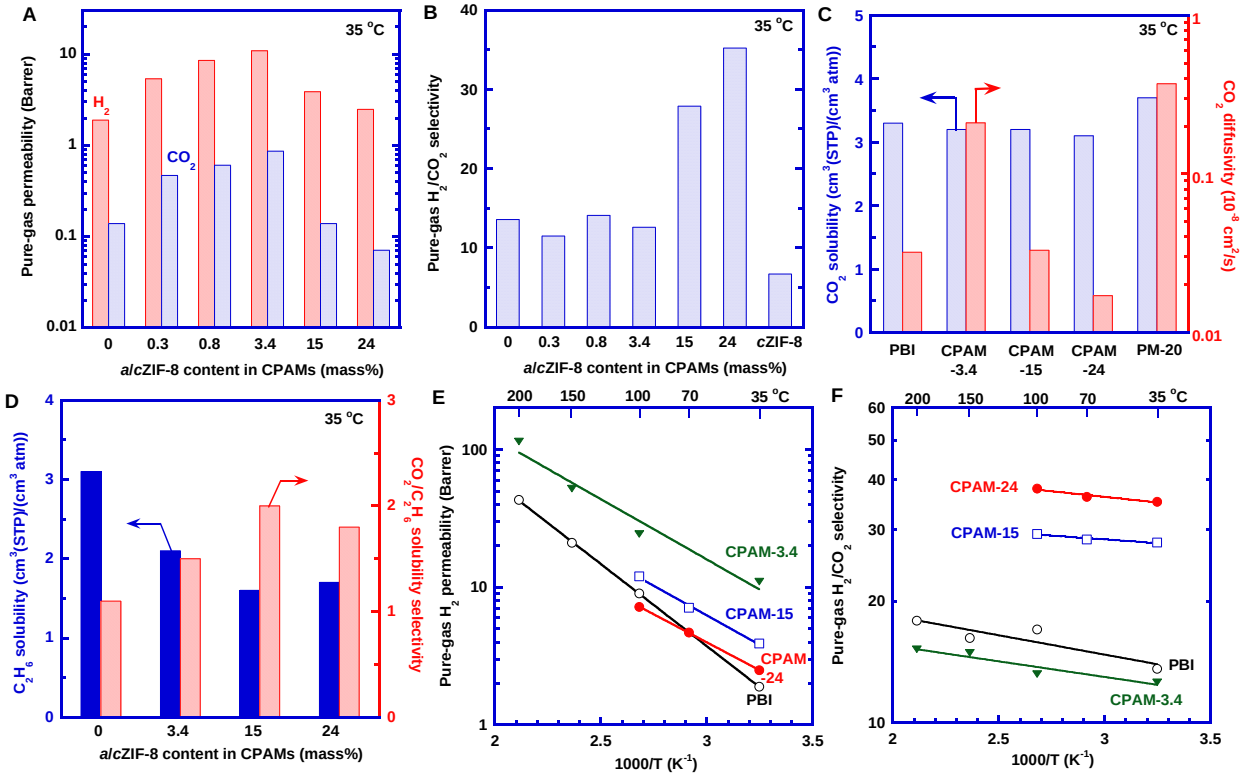

Figure 4. Pure-gas transport properties of CPAMs. (A) H_2 and CO_2 permeability at 35 °C; (B) H_2/CO_2 selectivity at 35 °C; (c) CO_2 solubility and diffusivity at 35 °C; (D) C_2H_6 solubility and CO_2/C_2H_6 solubility selectivity at 35 °C; Effect of temperature on (E) H_2 permeability and (F) H_2/CO_2 selectivity.

Figure 4B shows that the H_2/CO_2 selectivity remains constant as the *a*/*c*ZIF-8 content increases to 3.4 mass% before increasing significantly, which is consistent with the dominant effect of strongly size-sieving *a*ZIF-8 at high Zn contents. Particularly, CPAM-15 and CPAM-24 contain fully cross-linked PBI and thus strong size-sieving ability. Notably, ZIF-8 exhibits H_2/CO_2 selectivity of 6.7,[9b, 15, 30] lower than PBI (14) and the PMs (Table S6 and Figure S4). Therefore,

the constant selectivity for the CPAMs with low *a*/*c*ZIF-8 loadings reflects the compromise between *c*ZIF-8 (lowering the selectivity) and *a*ZIF-8 (cross-linking and enhancing the selectivity).

Gas permeability is usually decoupled into gas solubility and diffusivity to fully elucidate the transport mechanism. Figure 4C shows that PM-20 has a slightly higher CO_2 solubility than PBI because of the high porosity and thus high gas sorption of ZIF-8. In contrast, CPAMs exhibit CO_2 solubility similar to PBI, which can be ascribed to the cross-linking by *a*ZIF-8 and thus reduced free volume for gas sorption. Interestingly, C_2H_6 solubility decreases with increasing the *a*/*c*ZIF-8 loading before leveling off because the decreased free volume has more impact on the larger C_2H_6 than CO_2 (cf. Figure 4D). Consequently, CO_2/C_2H_6 solubility selectivity increases with increasing the *a*/*c*ZIF-8 loading at both 35 °C (Figure 4D) and 100 °C (Table S7).

As the ZIF-8 content has a negligible effect on CO_2 solubility in the CPAMs, the change in the gas permeability is mainly derived from gas diffusivity. CO_2 diffusivity increases from PBI to CPAM-3.4 before decreasing with increasing *a*/*c*ZIF-8 loading, reflecting the competing effects of the highly porous *c*ZIF-8 and low-free-volume *a*ZIF-8.

The molar ratios of the Zn^{2+} to 2-mIm were varied to understand their effect on the H_2/CO_2 separation properties at 35 °C, and the results are summarized in Table S6. First, the introduction of 2-mIm only in PBI does not affect the H_2/CO_2 separation properties because the 2-mIm does not interact with PBI to change the chain packing. Second, the addition of $Zn(NO_3)_2$ only does not affect the H_2/CO_2 separation properties, indicating that Zn^{2+} and PBI do not form *a*ZIF-8 without 2-mIm, presumably because the PBI cannot dissociate the $Zn(NO_3)_2$ without 2-mIm. Third, a sample (S3) containing the same amount of $Zn(NO_3)_2$ as CPAM-15 but higher 2-mIm content than CPAM-15 shows H_2/CO_2 selectivity (25) similar to and H_2 permeability (2.3 Barrer) lower than CPAM-15. Fourth, another sample (S4) with the ratio of $Zn(NO_3)_2$ to 2-mIm higher than CPAM-

24 displays higher H_2 permeability and lower H_2/CO_2 selectivity. These results showcase the synergy of $Zn(NO_3)_2$ and 2-mIm in influencing H_2/CO_2 separation properties, and higher ratio of $Zn(NO_3)_2$ to 2-mIm increases the H_2 permeability.

To confirm the generality of this approach, ZIF-7 and ZIF-67 in PBI were prepared via the in-situ growth method the same as that for ZIF-8, except that bIm (instead of 2-mIm) was used for ZIF-7, and $Co(NO_3)_2$ (instead of $Zn(NO_3)_2$) was used for ZIF-67 (Figure S3). Both samples exhibit H_2 permeability and H_2/CO_2 selectivity higher than PBI (Table S6), indicating the formation of the crystalline and amorphous ZIF-7 or ZIF-67, consistent with the CPAMs based on ZIF-8. For instance, ZIF-7/PBI displays H_2 permeability of 4.7 Barrer and H_2/CO_2 selectivity of 22, similar to CPAM-4.2.

Figure 4E,F exhibits the effect of temperature on pure-gas H_2/CO_2 separation properties in CPAMs. Gas permeability increases with increasing temperature, which can be described using the Arrhenius equation,[31] and the fitting parameters are recorded in Table S8. Increasing the *a*/*c*ZIF-8 content decreases the activation energy values ($E_{P,A}$) because of the increased content of *c*ZIF-8 NPs. Figure 4F shows that the H_2/CO_2 selectivity is independent of the temperature for all samples, and CPAM-24 exhibits the highest selectivity within the temperature range of 35-100 ℃. The results also confirm that the *a*/*c*ZIF-8 is stable at 200 ℃, consistent with the TGA curves (Figure 2C).

Superior H_2/CO_2 separation performance: Figure 5A compares the pure-gas separation properties of the CPAMs and PMs at 35 ℃.[32] CPAM-15 and CPAM-24 exhibit H_2/CO_2 separation properties surpassing 2008 Robeson's upper bound. The PMs show the separation properties approaching the upper bound, though the decrease in the selectivity with increasing the

*c*ZIF-8 loading is not desirable. Figure 5B also shows that the CPAMs exhibit separation properties above the upper bound at 100 °C.

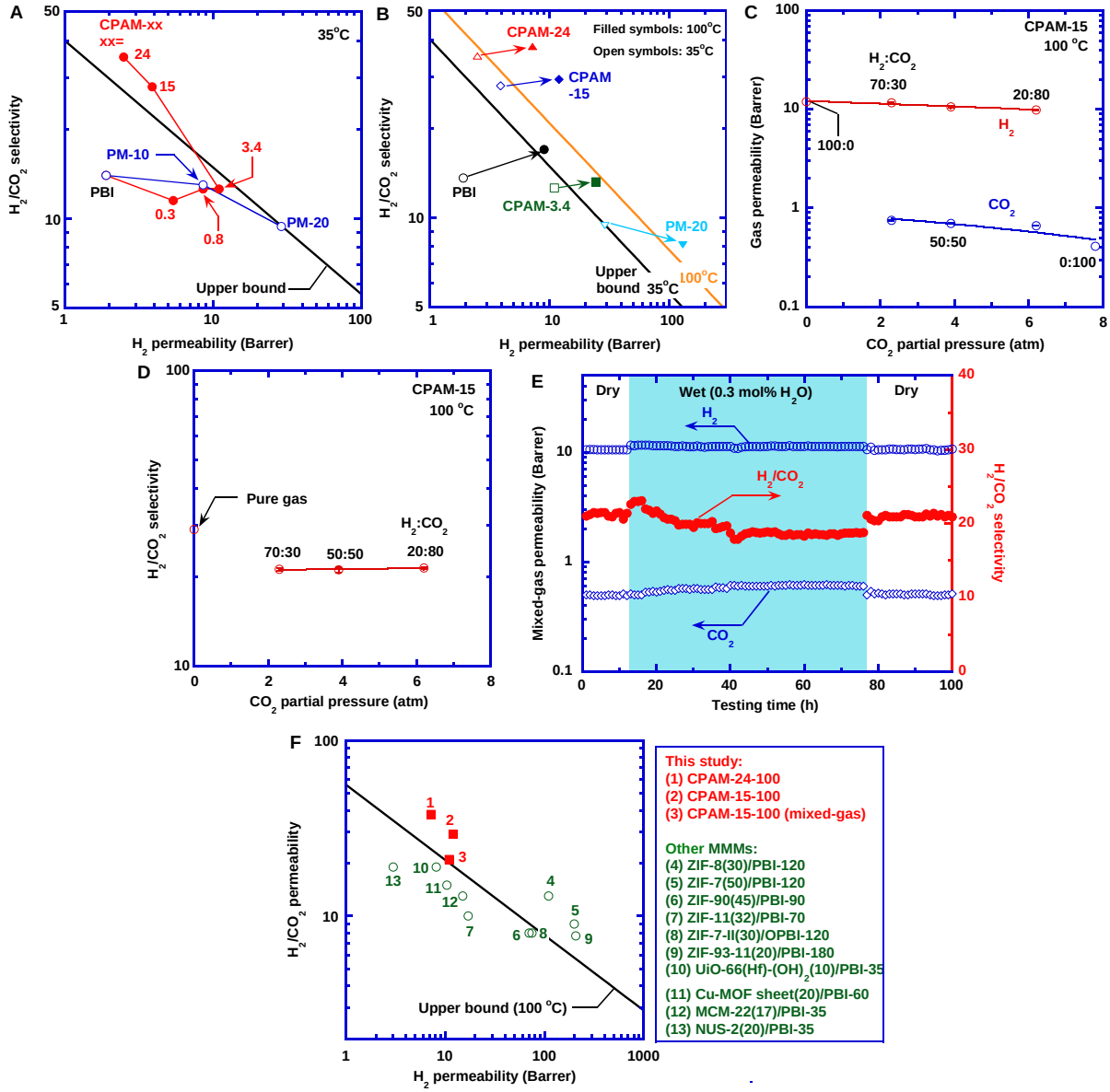

Figure 5. Superior H_2/CO_2 separation performance of the CPAMs. (A) Pure-gas H_2/CO_2 separation performance at 35 °C in the 2008 Robeson's upper bound. (B) Comparison of pure-gas H_2/CO_2 separation performance at 35 and 100 °C. (C) Mixed-gas H_2 and CO_2 permeability and (D) H_2/CO_2 selectivity at 6.5 atm and 100 °C as a function of the feed CO_2 partial pressure. (E) Long-term stability of CPAM-15 in dry-wet-dry conditions when challenged with H_2/CO_2 of 50:50 at 6.5 atm and 100 °C for 100 h. (F) Comparison of CPAM-15 and CPAM-24 with leading MMMs for H_2/CO_2 separation, including ZIF-8(30)/PBI,[14b] ZIF-7(50)/PBI,[33] ZIF-90(45)/PBI,[34] ZIF-11(32)/PBI,[35] ZIF-7-II(30)/OPBI,[36] ZIF-93-11(20)/PBI[37], UiO-66(Hf)–$(OH)_2$(10)/PBI,[38] Cu-

MOF sheet(20)/PBI,[39] MCM-22(17)/PBI,[40] NUS-2(20)/PBI.[41] The number of *ttt* after the sample name represents testing temperature (°C). The details are provided in Table S9.

CPAM-15 shows the best combination of H_2 permeability and H_2/CO_2 selectivity at 100 °C, and therefore, it was chosen to investigate the mixed-gas H_2/CO_2 separation performance and long-term stability. Three gas mixtures containing H_2/CO_2 of 70:30, 50:50, and 20:80 were used. Both H_2 and CO_2 permeability decrease with increasing CO_2 partial pressure because of the competitive sorption (Figure 5C). Interestingly, the mixed-gas H_2/CO_2 selectivity remains constant, suggesting the absence of CO_2 plasticization due to the low CO_2 sorption at high temperatures.[31] Nevertheless, the mixed-gas selectivity is lower than the pure-gas selectivity because of the competitive sorption, as observed for other MOF-based MMMs due to competitive sorption.[14b, 33]

CPAM-15 was also challenged with simulated syngas containing 50% H_2 and 50% CO_2 at 100 °C and 6.5 atm, as shown in Figure 5E. The film displays stable separation performance with the dry gas mixture for 12 h. When 0.3 mol% water vapor is introduced into the feed, both gas permeability and selectivity slightly decrease. After shifting back to the dry gas, the H_2/CO_2 separation properties return to the original values.

Figure 5F compares CPAM-15 and CPAM-24 with state-of-the-art MMMs for H_2/CO_2 separation.[14b, 33-41] CPAM-15 and CPAM-24 display competitive H_2/CO_2 separation performance and higher H_2/CO_2 selectivity due to the unique *a*ZIF-8 structure.[17,49,50,18,12,13,14] Unlike most approaches that are subject to the permeability-selectivity tradeoff, the in-situ growth of *a*/*c*ZIF-8 in functional polymers provides an effective route to simultaneously increase H_2 permeability and H_2/CO_2 selectivity. More importantly, compared with the conventional MMMs by post-synthesis mixing that often suffer from interfacial voids, the in-situ growth of the ZIFs in ligand-containing

polymers provides a facile route to fabricate defect-free membranes and can be used to produce membranes on a large scale using existing manufacturing processes.

3. Conclusion

We demonstrate a new concept of fabricating MMMs for gas separations by in situ synergistic growth of *c*ZIFs NPs and functional polymer-incorporated *a*ZIFs (CPAMs). The bIm groups on the PBI backbones with a structure similar to the ZIF-8 ligands (2-mIm) induce the formation of the aZIF-8. The formation of the *c*ZIFs is confirmed by the FTIR, WAXD, and SEM, and the formation of *a*ZIFs is validated by the FTIR, gel content, density, and TGA. The *c*ZIF-8 NPs render high gas permeability, while the *a*ZIF-8 cross-links the PBI chains and decreases the free volume, enhancing the H_2/CO_2 selectivity. As such, increasing the *a*/*c*ZIF-8 content can simultaneously improve H_2 permeability and H_2/CO_2 selectivity, overcoming the permeability/selectivity tradeoff of traditional MMMs. Increasing temperature increases gas permeability while retaining high H_2/CO_2 selectivity, and the CPAMs are stable at 200 ℃. CPAM-15 exhibits superior and stable H_2/CO_2 separation performance (H_2 permeability of 11 Barrer and H_2/CO_2 selectivity of 21) when challenged with simulated syngas at 100 ℃, surpassing Robeson's upper bound. This work may lead to a paradigm shift of designing polymers containing ligands for the optimized MMMs for a variety of other applications, such as fuel cell membranes, polymer electrolytes, electrocatalysts, and sensors.

4. Experimental

Materials. Celazole PBI powder (1.1 IV grade with Mw of 60 kDa) was purchased from PBI Performance Product Inc. (Charlotte, NC). Zinc nitrate hexahydrate [$Zn(NO_3)_2 \cdot 6H_2O$], 2-

methylimidazole ($C_4H_6N_2$, 2-mIm), and dimethylformamide (DMF) were acquired from Sigma-Aldrich Corporation (St. Louis, MO). Methanol (99.8%, MeOH) was obtained from Thermo Fisher Scientific (Waltham, MA). Gas cylinders of N_2, H_2, and CO_2 with ultrahigh purity were procured from Airgas Inc. (Buffalo, NY).

Synthesis of CPAMs via in-situ ZIF-8 growth. First, PBI was dissoved in DMF to form the solution of ~ 6 mass%.[31] Second, a desired amount of 2-mIm and DMF was added into the PBI solution followed by a solution of $Zn(NO_3)_2 \cdot 6H_2O$ (with a molar ratio of Zn^{2+} to 2-mIm of 1:8). The mixture was sonicated for 10 min at ≈ 23 ℃ for the in-situ growth of ZIF-8. Third, the solution was poured into a glass petri dish and dried in a N_2 oven at 60 ℃ for 12 h. The dried film was peeled off and further dried in a vacuum oven at 100 ℃ for 48 h. Finally, the film was immersed in 250 ml MeOH for 24 h to remove the non-reacted precursors before drying in the vacuum oven at 100 ℃ for 6 h.

Preparation of PMs via post-synthesis mixing approach. ZIF-8 NPs were synthesized following a rapid room-temperature synthesis method.[15] To prepare PMs, the desired amount of ZIF-8 NPs was first dispersed in DMF (3 g), and the mixture was then added into the ~6 mass% PBI/DMF solution (3 g). Second, the solution was poured into a glass petri dish and dried in N_2 at 60 ^oC for 12 h. Finally, the dried film was peeled off and further dried in a vacuum oven at 100 ^oC for 48 h.

Characterization of the MMMs. Attenuated total reflection-FTIR (ATR-FTIR) was performed at wavenumbers from 600 to 2000 cm^{-1} at a resolution of 1 cm^{-1} using a vertex 70 Bruker spectrometer (Billerica, MA). A Rigaku Ultima IV X-ray diffractometer (Rigaku Analytical Devices, Wilmington, MA) was used to obtain WAXD patterns. The diffractometer has a CuKα x-ray wavelength of 1.54 Å and was operated in the range of 5–40° at 1 °/min.

Thermogravimetric analysis of the samples was conducted using an SDT Q600 thermogravimetric analyzer (TA Instruments, New Castle, DE) at 10 ℃/min from 23 to 800 ℃ with N_2 flow.

To determine the content of Zn atom and 2-mIm and their distributions in the CPAMs, 4 pieces of film samples for each CPAM were treated at 450 ℃ in a furnace (MTI Corporation, Richmond, CA) with a N_2 flow of 200 mL/min for 1 h. The ramping rate was 10 ℃/min. The sample was move from the furnace after cooling down, and the mass loss was calculated by comparing the weights before and after the treatment. Then, the treated samples were exposed under air and burned at 800 ℃ ramped up by 10 ℃/min. The final ash was ZnO, and its content was measured. Then, Zn and 2-mIm contents can be derived using Eq. S1-2. Based on the mass loss at 450 ℃, *c*ZIF-8 and *a*ZIF-8 contents can be calculated using Eq. S3-6.

The film density (ρ_m) was calculated using its weight in the air and iso-octane based on Archimedes' principle.[31] The gel content (w_{gel}) of the samples is calculated using the following equation:[29]

$$w_{gel} = \frac{m_1}{m_0} \times 100\% \quad (1)$$

where m_0 is the mass of the sample, and m_1 is the dry mass of the insoluble remainings (i.e., gels) after immersion in DMF to extract the sol at 35 ℃ for 24 h.

The mechanical properties of samples were determined at 100 ℃ using static tensile loading with a dynamic mechanical analysis (DMA, Q800 TA Instrument). Uniaxial tensile loading on the sample stripes (20 mm × 3 mm) was carried out with an initial strain of 0.1% at a constant strain rate of 1.0 %/min till the sample fractured. The Young's modulus of the samples was determined from the elastic deformation region of the stress-strain curve (which typically occurs within 1.0 % strain). The tensile strength and fracture strain of samples were also determined according to the stress-strain curve.

A focused ion beam scanning electron microscope (FIB-SEM, Carl Zeiss Auriga CrossBeam, Germany) was used to observe the cross-section of the samples. An energy-dispersive X-ray spectrometer (EDS, Oxford Instruments, Abingdon, UK) was used to analyze the elemental distribution. ZIF-8 NPs and PM-5.8 samples were characterized using a scanning transmission electron microscope (FEI Talos F200X; 200 kV; equipped with the EDS elemental mapping capability). The cross-sectional TEM samples were prepared by the standard in-situ lift-out procedure using Ga ion milling in an FIB system (FEI Helios 600 Nanolab).

Pure-gas H_2 and CO_2 permeability was determined using a constant-volume and variable-pressure system at various feed pressures and temperatures.[15, 31] Thin films were masked before the installation in the permeation cell to avoid damage by the gaskets, and the gas flux was measured from the steady-state rate of the pressure increase in the downstream volume. Pure-gas CO_2 and C_2H_6 sorption isotherms were determined using a gravimetric sorption analyzer (IGA 001, Hiden Isochema Ltd., Warrington, UK).[15]

Mixed-gas permeability was determined using a constant-pressure and variable-volume apparatus at various feed pressures and temperatures.[29, 31] Gas mixtures were prepared by in-line mixing, and N_2 was used as the sweep gas on the permeate side. Gas permeability of a sample with an active area of A_m and thickness of l can be calculated using the following equation:

$$P_A = \frac{x_A S l}{x_{sweep} A_m (p_{2,A} - p_{1,A})} \quad (2)$$

where S is the flow rate of the N_2 sweep gas, and $p_{2,A}$ and $p_{1,A}$ are the partial pressure of gas component A in the feed and permeate, respectively. x_A and x_{sweep} are the mole fraction of gas component A and N_2 in the sweep-out stream, respectively

Supporting Information

Supporting Information is available from the Wiley Online Library.

Acknowledgments
This work was funded by the U.S. Department of Energy (DOE) (DE-FE0031636) and the U.S. National Science Foundation (NSF, 1804996). This research used the Materials Synthesis and Characterization facility of the Center for Functional Nanomaterials, which is a U.S. DOE Office of Science Facility, at Brookhaven National Laboratory under Contract No. DE-SC0012704.

Leiqing Hu and Vinh T. Bui contributed equally to this work.

Conflict of Interest
The authors declare no conflict of interest.

Keywords
Mixed matrix membranes, amorphous metal-organic frameworks, in-situ growth, H_2/CO_2 separation, carbon capture

Received: ((will be filled in by the editorial staff))
Revised: ((will be filled in by the editorial staff))
Published online: ((will be filled in by the editorial staff))

References

[1] a) J. Wu, C. Liang, A. Naderi, T. Chung, *Adv. Mater.* **2021**, 2105156; b) L. Zhu, L. Huang, S. R. Venna, A. Blevins, Y. Ding, D. Hopkinson, M. T. Swihart, H. Lin, *ACS Nano* **2021**, 15, 12119; c) L. F. Villalobos, M. T. Vahdat, M. Dakhchoune, Z. Nadizadeh, M. Mensi, E. Oveisi, D. Campi, N. Marzari, K. V. Agrawal, *Sci. Adv.* **2020**, 6, eaay9851; d) L. Zhu, D. Yin, Y. Qin, S. Konda, S. Zhang, A. Zhu, S. Liu, T. Xu, M. T. Swihart, H. Lin, *Adv. Funct. Mater.* **2019**, 29, 1904357.
[2] a) Y. Han, W. S. Ho, *J. Membr. Sci.* **2021**, 628, 119244; b) L. Hu, S. Pal, H. Nguyen, V. Bui, H. Lin, *J. Polym. Sci.* **2020**, 58, 2467.
[3] a) H. Park, J. Kamcev, L. M. Robeson, M. Elimelech, B. D. Freeman, *Science* **2017**, 356, eaab0530; b) L. Zhu, M. Swihart, H. Lin, *Energy Environ. Sci.* **2018**, 11, 94.
[4] R. M. De Vos, H. Verweij, *Science* **1998**, 279, 1710.
[5] M. Dakhchoune, L. F. Villalobos, R. Semino, L. Liu, M. Rezaei, P. Schouwink, C. E. Avalos, P. Baade, V. Wood, Y. Han, *Nat. Mater.* **2021**, 20, 362.
[6] a) H. Guo, G. Kong, G. Yang, J. Pang, Z. Kang, S. Feng, L. Zhao, L. Fan, L. Zhu, A. Vicente, *Angew. Chem. Int. Ed.* **2020**, 59, 6284; b) H. Li, Z. Song, X. Zhang, Y. Huang, S. Li, Y. Mao, H. J. Ploehn, Y. Bao, M. Yu, *Science* **2013**, 342, 95.
[7] a) L. Lei, F. Pan, A. Lindbrathen, X. Zhang, M. Hillestad, Y. Nie, L. Bai, X. He, M. D. Guiver, *Nat. Commun.* **2021**, 12, 268; b) L. Hu, V. T. Bui, A. Krishnamurthy, S. Fan, W. Guo, S. Pal, X. Chen, G. Zhang, Y. Ding, R. P. Singh, M. Lupion, H. Lin, **2021**, submitted.
[8] Y. Peng, Y. Li, Y. Ban, H. Jin, W. Jiao, X. Liu, W. Yang, *Science* **2014**, 346, 1356.
[9] a) T. Lee, A. Ozcan, I. Park, D. Fan, J. Jang, P. G. M. Mileo, S. Yoo, J. Roh, J. Kang, B. Lee, Y. Cho, R. Semino, H. Kim, G. Maurin, H. Park, *Adv. Funct. Mater.* **2021**, 31; b) Y. Cheng, Y. Ying, S. Japip, S. Jiang, T. S. Chung, S. Zhang, D. Zhao, *Adv. Mater.* **2018**, 30, 1802401; c) C. Ma, J. J. Urban, *Adv. Funct. Mater.* **2019**, 29, 1903243; d) M. R. A. Hamid, S. Park, J. S. Kim, Y. M. Lee, H. K. Jeong, *J. Mater. Chem. A* **2019**, 7, 9680.
[10] Y. Ji, B. Gu, S. Xie, M. Yin, W. Qian, Q. Zhao, W. Hung, K. R. Lee, Y. Zhou, Q. An, C. Gao, *Adv. Mater.* **2021**, 33.

[11]Y. Ye, L. Gong, S. Xiang, Z. Zhang, B. Chen, *Adv. Mater.* **2020**, 32, 1907090.
[12] J. M. Whiteley, P. Taynton, W. Zhang, S. H. Lee, *Adv. Mater.* **2015**, 27, 6922.
[13] F. Zhang, Y. Feng, M. Qin, L. Gao, Z. Li, F. Zhao, Z. Zhang, F. Lv, W. Feng, *Adv. Funct. Mater.* **2019**, 29, 1901383.
[14] a) Q. Qian, P. A. Asinger, M. J. Lee, G. Han, K. Mizrahi Rodriguez, S. Lin, F. M. Benedetti, A. X. Wu, W. S. Chi, Z. P. Smith, *Chem. Rev.* **2020**, 120, 8161; b) T. Yang, G. Shi, T. S. Chung, *Adv. Energy Mater.* **2012**, 2, 1358; c) X. Ma, X. Wu, J. Caro, A. Huang, *Angew. Chem.* **2019**, 131, 16302; d) S. Japip, K. S. Liao, T. S. Chung, *Adv. Mater.* **2017**, 29, 1603833.
[15] L. Hu, J. Liu, L. Zhu, X. Hou, L. Huang, H. Lin, J. Cheng, *Sep. Purif. Technol.* **2018**, 205, 58.
[16] a) H. Kwon, H.-K. Jeong, *J. Am. Chem. Soc.* **2013**, 135, 10763; b) X. Ma, P. Kumar, N. Mittal, A. Khlyustova, P. Daoutidis, K. A. Mkhoyan, M. Tsapatsis, *Science* **2018**, 361, 1008; c) A. M. Marti, S. R. Venna, E. A. Roth, J. T. Culp, D. P. Hopkinson, *ACS Appl. Mater. Interfaces* **2018**, 10, 24784; d) L. Ma, F. Svec, Y. Lv, T. Tan, *J. Mater. Chem. A* **2019**, 7, 20293.
[17] a) J. Campbell, G. Székely, R. Davies, D. C. Braddock, A. G. Livingston, *J. Mater. Chem. A* **2014**, 2, 9260; b) S. Park, K. Cho, H.-K. Jeong, *J. Mater. Chem. A* **2020**, 8, 11210.
[18] a) Y. H. Wang, H. Fin, Q. Ma, K. Mo, H. Z. Mao, A. Feldhoff, X. Z. Cao, Y. S. Li, F. S. Pan, Z. Y. Jiang, *Angew. Chem. Int. Ed.* **2020**, 59, 4365; b) J. Fonseca, T. H. Gong, L. Jiao, H. L. Jiang, *J. Mater. Chem. A* **2021**, 9, 10562; c) T. D. Bennett, A. K. Cheetham, *Acc. Chem. Res.* **2014**, 47, 1555.
[19] M. A. Mohamed, J. Jaafar, A. Ismail, M. Othman, M. Rahman, in *Membrane Characterization*, Elsevier **2017**, p. 3.
[20] Y. Hu, H. Kazemian, S. Rohani, Y. Huang, Y. Song, *Chem. Comm.* **2011**, 47, 12694.
[21] A. Kertik, L. H. Wee, M. Pfannmoller, S. Bals, J. A. Martens, I. F. J. Vankelecom, *Energy Environ. Sci* **2017**, 10, 2342.
[22] X. Cui, Y. Song, J. Wang, J. Wang, Q. Zhou, T. Qi, G. Li, *Polymer* **2019**, 174, 143.
[23] A. Shimazu, T. Miyazaki, K. Ikeda, *J. Membr. Sci.* **2000**, 166, 113.
[24] J. B. James, Y. Lin, *J. Phys. Chem. C* **2016**, 120, 14015.
[25] J. A. Thompson, C. R. Blad, N. A. Brunelli, M. E. Lydon, R. P. Lively, C. W. Jones, S. Nair, *Chem. Mater.* **2012**, 24, 1930.
[26] a) M. Lee, H. Kwon, H. Jeong, *Angew. Chem. Int. Ed.* **2018**, 57, 156; b) J. B. James, L. Lang, L. Meng, J. Y. S. Lin, *ACS Appl. Mater. Interfaces* **2020**, 12, 3893; c) M. Kim, J. F. Cahill, H. H. Fei, K. A. Prather, S. M. Cohen, *J. Am. Chem. Soc.* **2012**, 134, 18082.
[27] W. Zhou, H. Wu, M. R. Hartman, T. Yildirim, *J. Phys. Chem. C* **2007**, 111, 16131.
[28] E. Mahdi, J. Tan, *J. Membr. Sci.* **2016**, 498, 276.
[29] L. Zhu, M. Swihart, H. Lin, *J. Mater. Chem. A* **2017**, 5, 19914.
[30] C. Zhang, R. P. Lively, K. Zhang, J. R. Johnson, O. Karvan, W. J. Koros, *J. Phys. Chem. Lett.* **2012**, 3, 2130.
[31] L. Hu, V. T. Bui, L. Huang, R. P. Singh, H. Lin, *ACS Appl. Mater. Interfaces* **2021**, 13, 12521.
[32] L. M. Robeson, *J. Membr. Sci.* **2008**, 320, 390.
[33] T. Yang, Y. Xiao, T. S. Chung, *Energy Environ. Sci* **2011**, 4, 4171.
[34] T. Yang, T. S. Chung, *J. Mater. Chem. A* **2013**, 1, 6081.
[35] J. Sánchez-Laínez, B. Zornoza, C. Téllez, J. Coronas, *J. Mater. Chem. A* **2016**, 4, 14334.
[36] S. Yang, Y. Wang, P. Lu, H. Jin, F. Pan, Z. Shi, X.-s. Jiang, C. Chen, Z. Jiang, Y. Li, *ACS Appl. Mater. Interfaces* **2020**, 12, 55308.
[37] J. Sánchez-Laínez, B. Zornoza, A. F. Orsi, M. M. Łozińska, D. M. Dawson, S. E. Ashbrook, S. M. Francis, P. A. Wright, V. Benoit, P. L. Llewellyn, *Chem. Eur. J.* **2018**.
[38] Z. Hu, Z. Kang, Y. Qian, Y. Peng, X. Wang, C. Chi, D. Zhao, *Ind. Eng. Chem. Res.* **2016**, 55, 7933.
[39] Z. Kang, Y. Peng, Z. Hu, Y. Qian, C. Chi, L. Y. Yeo, L. Tee, D. Zhao, *J. Mater. Chem. A* **2015**, 3, 20801.
[40] S. Choi, J. Coronas, Z. Lai, D. Yust, F. Onorato, M. Tsapatsis, *J. Membr. Sci.* **2008**, 316, 145.
[41] Z. Kang, Y. Peng, Y. Qian, D. Yuan, M. A. Addicoat, T. Heine, Z. Hu, L. Tee, Z. Guo, D. Zhao, *Chem. Mater.* **2016**, 28, 1277.

Table of Contents Entry

In situ growth of ZIF-8 in polybenzimidazole (PBI) generates bimodal free volumes from tightly packed amorphous ZIF-8 (induced by PBI) and highly porous crystalline ZIF-8. Such hierarchical nanostructures improves H_2 permeability and H_2/CO_2 selectivity simultaneously, overcoming the permeability/selectivity tradeoff. The study unveils the important yet neglected role of functional polymers in designing a new platform of mixed matrix materials for a broad range of applications.

Keywords: Mixed matrix membranes · amorphous metal-organic frameworks · in-situ growth · H_2/CO_2 separation · carbon capture

Leiqing Hu, Vinh T Bui, Sankhajit Pal, Wenji Guo, Ashwanth Subramanian, Kisslinger Kim, Shouhong Fan, Chang-Yong Nam, Yifu Ding, Haiqing Lin

In situ synergistic growth of crystalline and polymer-incorporated amorphous ZIF-8 in polybenzimidazole achieving hierarchical nanostructrues for H_2/CO_2 separation